

## Transformation optics and hidden symmetries

Matthias Kraft, J. B. Pendry, S. A. Maier, and Yu Luo\*

*Blackett Laboratory, Department of Physics, Imperial College London, London SW7 2AZ, United Kingdom*

(Received 10 March 2014; revised manuscript received 5 June 2014; published 20 June 2014)

Symmetry plays an important role in physics providing a means of classification and a route to understanding. Here we show that an apparently unsymmetrical structure, in our example an ellipse/spheroid, has a more symmetrical partner with an identical spectrum and through which its electromagnetic properties can be classified and calculated analytically. We use the powerful tool of transformation optics to establish this relationship which has wide application beyond the simple example we give in this paper.

DOI: [10.1103/PhysRevB.89.245125](https://doi.org/10.1103/PhysRevB.89.245125)

PACS number(s): 73.20.Mf, 71.36.+c, 42.70.-a

### I. INTRODUCTION

In this paper we address the issue of hidden symmetries in plasmonic systems. Sophisticated computer codes such as COMSOL enable us to solve for electromagnetic fields in complex geometries but powerful as they may be they often provide little insight into how the solutions arise and therefore cramp our imagination. Analytic solutions where they are to be found arise from a particular insight and can show the way forward to addressing the problem in hand. The new tool of transformation optics greatly assists the analytic approach. Given a solution of Maxwell's equations for a particular geometry, we can demand that the fields be distorted to choice and given the coordinate transformation from the original to distorted frames we can calculate the values of permittivity and permeability that satisfy Maxwell's equations in the distorted system [1–5]. Given the infinite range of transformations available to us, a single simple system and its electromagnetic fields can be transformed into wildly different shapes. In this way we have shown how a wide variety of singular plasmonic structures that concentrate energy at singular points are related to a single “mother” system [6,7]. Here we use transformation optics to address the issue of symmetry. The modes of a system can be classified by the symmetry of the system. For example a system that is translationally invariant has eigenstates that are Bloch waves classified by their wave vector [8–10]. Not only does this expedite analytic solutions but identification of the underlying structure of the modes inspires our understanding: the electronic structure of solids would be far less advanced without the aid of translational symmetry. Given a highly symmetrical system, whose eigenstates we can classify, that symmetry can be hidden by imposing an unsymmetrical coordinate transformation. However, the classification remains because the eigenmodes of the transformed system are given by the original classified modes. Of course it is not always possible to relate an arbitrary unsymmetrical system to one that is more symmetrical but there are many instances where symmetry does lie hidden. Here we give as an example one of the simplest: an ellipse/spheroid which can be transformed into two concentric circles/spheres creating continuous rotational symmetry where none previously existed. We treat both the two-dimensional (2D) and three-dimensional (3D) cases.

### II. TRANSFORMATION OF THE GEOMETRY

The systems we are interested in are an elliptic cylinder with infinite extent in the  $z'$  direction and a spheroid with rotational symmetry around the  $z'$  axis. Since we are dealing with an elliptic cylinder of infinite length, this system is equivalent to a two-dimensional ellipse. We assume that both ellipse and spheroid are made out of metal with permittivity  $\epsilon'_m$  and permeability  $\mu'_m = 1$ , and are immersed in a dielectric of permittivity  $\epsilon'_d$  and permeability  $\mu'_d = 1$ . The incident illumination is a plane wave, and in the quasistatic approximation it can be taken as a uniform electric field. Let us consider the 2D case first. The source potential (in the original coordinate frame) can be written as

$$\phi'_{s,2d} = -E_{x'}x' - E_{y'}y', \quad (1)$$

where  $E_{x'}$  and  $E_{y'}$  are the electric field components along the  $x'$  and  $y'$  axes, respectively. We now apply the transformation

$$\zeta' = \frac{c'}{2} \left( \zeta + \frac{1}{\zeta} \right) \quad (2)$$

with  $\zeta' = x' + iy'$ ,  $\zeta = x + iy$ , and  $c' \in +\mathbb{R}$ , which is essentially a Joukowski transformation [11]. The real and imaginary parts transform as

$$x' = \frac{c'}{2} x \left( 1 + \frac{1}{x^2 + y^2} \right), \quad (3)$$

$$y' = \frac{c'}{2} y \left( 1 - \frac{1}{x^2 + y^2} \right). \quad (4)$$

Here and in the following, primed quantities refer to the ellipse/spheroid geometry and unprimed ones to the transformed space. Starting with an ellipse in the primed frame, with semimajor axis  $a' = c' \cosh(u'_0)$ , semiminor axis  $b' = c' \sinh(u'_0)$ , and centered at the origin, one can show that this transforms to an annulus with inner and outer radii  $R_{\text{in}} = a' - b' = e^{-u'_0}$  and  $R_{\text{out}} = a' + b' = e^{u'_0}$ , respectively. One could go on to transform the annulus to an infinite metal slab [12], which is a problem that has been discussed extensively in the literature [13,14], but we will work in the rotationally symmetric annulus geometry. Since the transformation in Eq. (2) is conformal, the permittivity and source potential transform trivially as  $\epsilon'_d = \epsilon_d$ ,  $\epsilon'_m = \epsilon_m$ , and  $\phi'_{s,2d}(x',y') = \phi_{s,2d}(x,y)$  [6,15]. Using this together with the transformation in Eq. (2), the source potential in the transformed frame can

\*Corresponding author: [y.luo09@imperial.ac.uk](mailto:y.luo09@imperial.ac.uk)

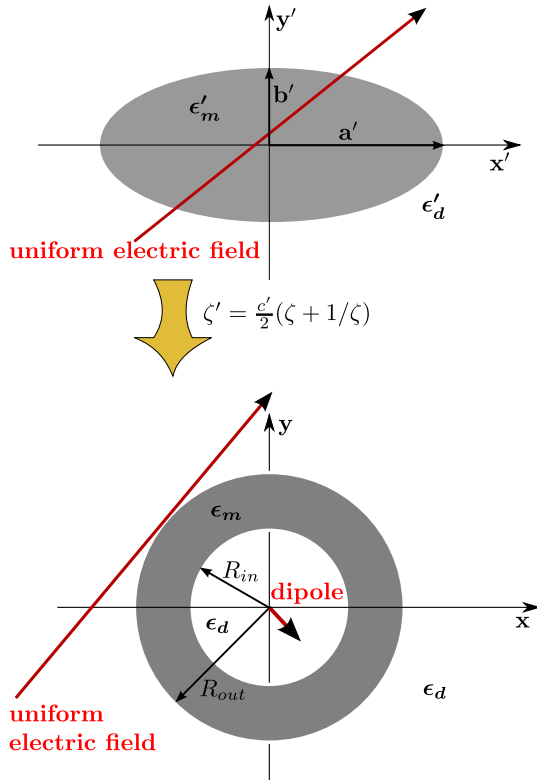


FIG. 1. (Color online) Schematic illustration of the transformation in Eq. (2) applied to a metal ellipse in a uniform electric field. The transformed metal annulus is rotationally symmetric.

be deduced:

$$\phi_s(x, y) = -\frac{c'}{2} \mathbf{E}'_0 \cdot \mathbf{r} + \frac{\mathbf{p} \cdot \mathbf{r}}{2\pi \epsilon_0 r^2}, \quad (5)$$

where we defined three vectors:

$$\mathbf{E}'_0 = \begin{bmatrix} E_{x'} \\ E_{y'} \end{bmatrix}, \quad \mathbf{r} = \begin{bmatrix} x \\ y \end{bmatrix}, \quad \mathbf{p} = \pi \epsilon_0 c' \begin{bmatrix} E_{x'} \\ -E_{y'} \end{bmatrix}. \quad (6)$$

Thus, the uniform electric field  $\mathbf{E}'_0$  (in the original frame) transforms to a uniform electric field scaled by  $c'/2$ , plus a line dipole at the origin with a dipole moment  $\mathbf{p}$ . The result of this transformation is shown schematically in Fig. 1. Similarly, one can show that a dipole in the ellipse's geometry transforms to two dipoles in the transformed annulus space (see Appendix A).

An analogous transformation in 3D transforms a spheroid to a concentric spherical shell. Specifically, for a prolate spheroid we can use  $\rho' = \frac{1}{2}(r - \frac{1}{r}) \sin(\theta)$ ,  $z' = \frac{1}{2}(r + \frac{1}{r}) \cos(\theta)$ , and  $\phi' = \phi$ , where  $r, \theta$ , and  $\phi$  are the standard spherical polar coordinates. The transformation of the source potential is analogous to the 2D case; however the permittivity and permeability change according to the rules of transformation optics [1,2,4,5]:

$$\epsilon^{ij} = \det(J)^{-1} J_{i'}^i J_{j'}^j \epsilon'^{i'j'}, \quad (7)$$

$$\mu^{ij} = \det(J)^{-1} J_{i'}^i J_{j'}^j \mu'^{i'j'}, \quad (8)$$

where  $J$  is the Jacobian transformation matrix. In our case this leads to

$$\epsilon_{r,d/m}^p = \epsilon_{\theta,d/m}^p = \frac{1-r^2}{2r^2} \epsilon'_{d/m}, \quad (9)$$

$$\mu_{r,d/m}^p = \mu_{\theta,d/m}^p = \frac{1-r^2}{2r^2}, \quad (10)$$

$$\epsilon_{\phi,d/m}^p = \frac{1+r^4-2r^2 \cos(2\theta)}{2r^2(1-r^2)} \epsilon'_{d/m}, \quad (11)$$

$$\mu_{\phi,d/m}^p = \frac{1+r^4-2r^2 \cos(2\theta)}{2r^2(1-r^2)}. \quad (12)$$

Similarly, for an oblate spheroid we can use the transformation  $\rho' = \frac{1}{2}(r + \frac{1}{r}) \sin(\theta)$ ,  $z' = \frac{1}{2}(r - \frac{1}{r}) \cos(\theta)$ , and  $\phi' = \phi$  and get

$$\epsilon_{r,d/m}^o = \epsilon_{\theta,d/m}^o = -\frac{1+r^2}{2r^2} \epsilon'_{d/m}, \quad (13)$$

$$\mu_{r,d/m}^o = \mu_{\theta,d/m}^o = -\frac{1+r^2}{2r^2}, \quad (14)$$

$$\epsilon_{\phi,d/m}^o = -\frac{1+r^4+2r^2 \cos(2\theta)}{2r^2(1+r^2)} \epsilon'_{d/m}, \quad (15)$$

$$\mu_{\phi,d/m}^o = -\frac{1+r^4+2r^2 \cos(2\theta)}{2r^2(1+r^2)}. \quad (16)$$

It should be stressed that although 3D transformations result in permittivity/permeability that depend on  $r$  and  $\theta$ , the eigenmodes supported by the system can still be characterized by spherical harmonics for the angular part (i.e.,  $\theta$  and  $\phi$ ) and assigned “quantum” numbers,  $l, m$ . The spatial dependence in  $\epsilon$  and  $\mu$  only affects the solution for the radial part (i.e.,  $r$ ). This is a subtle point which contrasts a previous study [16] and will be explained in the Appendix C. Good “quantum” numbers in the transformed geometry will remain good “quantum” numbers upon transforming back to the original. Furthermore, the geometries in the transformed space possess rotational (2D) and spherical (3D) symmetry. The transformations thus reveal a “hidden” symmetry in the ellipse/spheroid geometry, which helps to shed light on the optical response of the nanoparticles.

### III. PLASMON MODE STRUCTURE AND SYMMETRIES

With the geometries and source potential in the transformed space known, we can calculate the system's properties in the quasistatic limit by solving [17]

$$\nabla \cdot (\bar{\epsilon} \cdot \nabla \phi) = 0, \quad (17)$$

and demanding continuity of the tangential component of the electric field and continuity of the normal component of the electric displacement across the metal/dielectric boundary. In the 2D case this reduces to solving Laplace's equation in polar coordinates, which is a laborious but straightforward task, so we shall only give the results here. The 3D case is more complicated, but can also be solved analytically with TO. We refer the reader to the Appendix C for details. In both cases

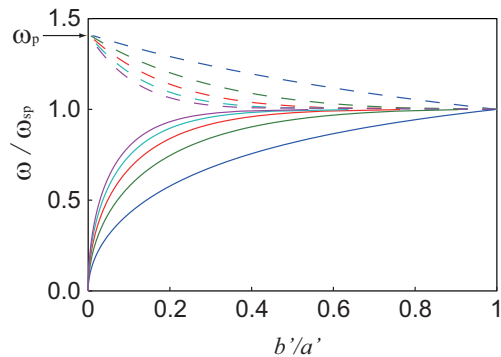


FIG. 2. (Color online) Shift of the plasmon resonance frequencies as a function of the ratio of semiminor to semimajor axis of the ellipse. The dashed lines correspond to (in descending order) the  $m = 1, 2, 3, 4, 5$  odd plasmon modes and the solid lines correspond to (in ascending order) the  $m = 1, 2, 3, 4, 5$  even plasmon modes. We used the Drude model with  $\omega_p = 8$  eV and negligible losses and defined the surface plasma frequency  $\omega_{sp} = \omega_p / \sqrt{2}$ .

we find resonance conditions for the excitation of localized surface plasmon modes.

In 2D cases, the resonance condition is split into even and odd plasmon modes and reads

$$\tanh(mu_0) = -\frac{\varepsilon_d}{\varepsilon_m} \quad (18)$$

for even and

$$\tanh(mu_0) = -\frac{\varepsilon_m}{\varepsilon_d} \quad (19)$$

for odd modes, with  $u_0 = \tanh^{-1}(b'/a')$ . These are the conditions obtained for the annulus; however, by virtue of our transformation they are also the correct conditions for the ellipse. In the following we assume the annulus to be made of silver, immersed in the vacuum. Unless stated otherwise, we use a Drude model fit of Johnson and Christy's data [18] for the permittivity  $\varepsilon_m = 1 - \omega_p^2 / [\omega(\omega + i\gamma)]$  with  $\omega_p = 8$  eV and  $\gamma = 0.032$  eV.

The potential problem of a 2D ellipse in a constant electric field has been addressed before analytically [19] and numerically [20]. The modes of this system have also been studied in terms of the Mathieu function [21]. However, to the authors' best knowledge, the physical reason for the mode splitting has not been adequately discussed in the literature and neither has the equivalence of the annulus and ellipse system.

Figure 2 shows the resonance condition as a function of the ratio between semiminor and semimajor axis  $b'/a'$ . Note that in the limiting case  $b'/a' = 1$  (i.e., a cylinder), we recover the well-known result that all surface plasmon modes are degenerate at the surface plasma frequency [22]. In the opposite limit  $b'/a' \rightarrow 0$ , i.e., a thin strip, the splitting of the modes is most prominent with the odd modes shifting to the bulk plasma frequency  $\omega_p$  and the even modes shifting to zero frequency.

Figure 2 indicates that when a cylinder is deformed into an ellipse, the modes split into even and odd parities. The general splitting of the modes results from a breaking of rotational symmetry; however the modes specifically split into even

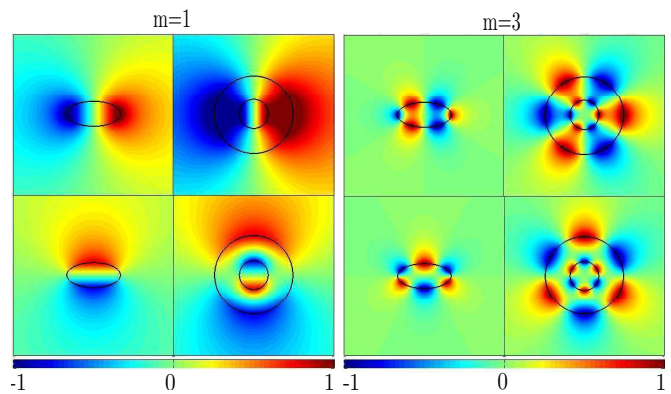


FIG. 3. (Color online) Imaginary part of the electrostatic potential at the  $m = 1$  (left) and  $m = 3$  (right) resonance. We show the potential for the 2D ellipse and the corresponding annulus geometry, as indicated. The top panel shows the even, the bottom panel the odd plasmon modes. The  $m = 1$  resonance has been excited by a plane wave with the source potential of Eq. (1) ( $E'_x = E'_y$ ) and the  $m = 3$  resonance by a dipole in the near field of the ellipse ( $\Delta'_x = \Delta'_y$ ; see Appendix A).

and odd parities because the ellipse still possesses two mirror planes.

As previously shown, the ellipse transforms to an annulus, which has the same plasmon mode structure as in Fig. 2. The annulus is a rotationally symmetric structure; thus the mode splitting in it is not owing to symmetry breaking. The reason for the mode splitting becomes evident from Fig. 3. It shows the electrostatic potential  $\phi'_{2d}$  at the  $m = 1$  (left) and  $m = 3$  (right) resonance for the ellipse and the corresponding one for the transformed annulus. We can see that there are localized surface plasmons excited at both inner and outer surfaces in the annulus geometry. These plasmons interact and hybridize, which leads to the formation of bonding and antibonding modes [23,24]. This is the physical reason for the splitting of the plasmon modes in the annulus geometry [23,24]. There is thus a clear connection between the breaking of rotational symmetry in the single surface elliptic geometry and plasmon hybridization in the two surface annulus geometry.

Next, let us turn our attention to 3D cases. As pointed out in the previous section, for the 3D spheroidal nanoparticles, the permittivity/permeability of the transformed annulus geometry is no longer homogeneous, but acquires a  $\theta$  dependence. However, this spatial dependence only adds a little complication to the problem, and the plasmon modes supported by the system can still be diagonalized by two quantum numbers, i.e., the total angular momentum  $l$  and the azimuthal angular momentum  $m$ . This is quite different from the case of the sphere pair in our previous study, where all the eigenmodes as a whole are described by a tridiagonal matrix [16]. Our detailed derivations provided in the Appendix C show that the resonance conditions for prolate and oblate spheroids are respectively given by

$$\frac{\varepsilon_m}{\varepsilon_d} = \frac{P_l^m(\tau) [i \frac{\pi}{2} P_l^{m'}(\tau) + Q_l^{m'}(\tau)]}{[i \frac{\pi}{2} P_l^m(\tau) + Q_l^m(\tau)] P_l^{m'}(\tau)}, \quad (20)$$

$$\frac{\varepsilon_m}{\varepsilon_d} = \frac{P_l^m(i\xi) [-i \frac{\pi}{2} P_l^{m'}(i\xi) + Q_l^{m'}(i\xi)]}{[-i \frac{\pi}{2} P_l^m(i\xi) + Q_l^m(i\xi)] P_l^{m'}(i\xi)}, \quad (21)$$

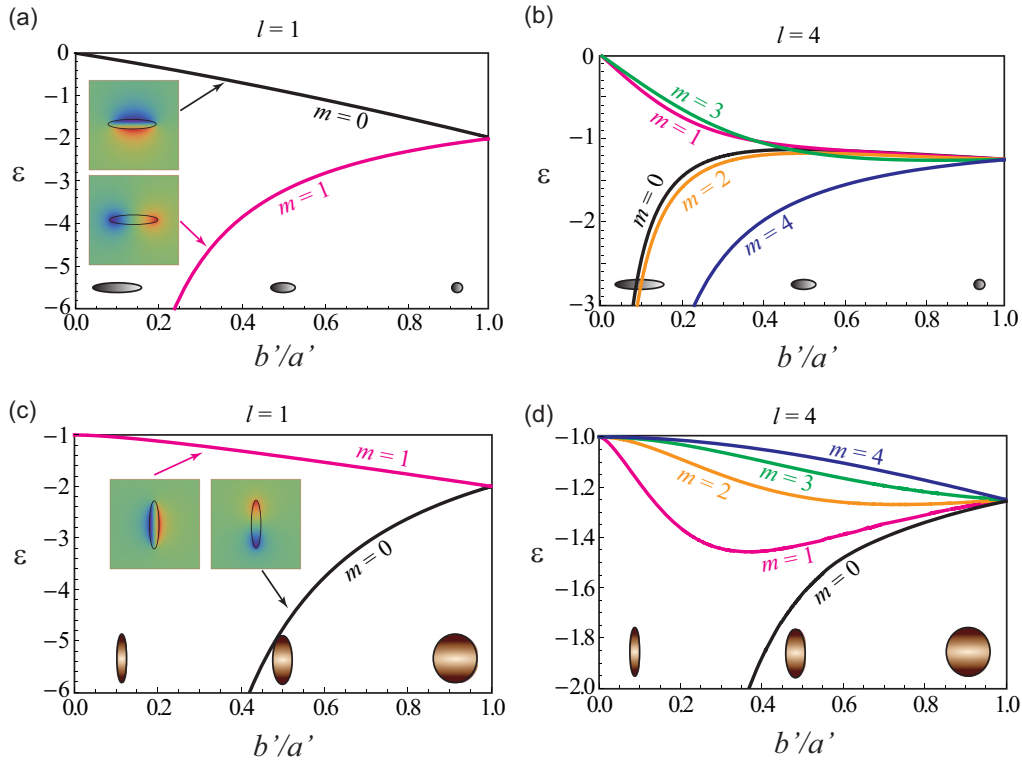


FIG. 4. (Color online) Shift of the plasmon resonance frequencies as a function of the ratio of semiminor to semimajor axis of the 3D spheroid; oblate (top) and prolate (bottom). The insets (left) show the electrostatic potential for their respective modes.

where  $\tau = (R^{\text{out}} + 1/R^{\text{out}})/2$  and  $\xi = (R^{\text{out}} - 1/R^{\text{out}})/2$ ;  $P_l^m(\cdot)$  and  $Q_l^m(\cdot)$  represent the associated Legendre polynomials of the first and second kind, respectively.

In the past, light scattering from spheroidal nanoparticles was studied using a spheroidal wave expansion [25–28] or shape perturbation method [29]. However, due to their slow convergence, these methods normally demand high computational resources in order to obtain a reasonable accuracy. Hence, discussions of plasmon resonances are generally restricted to dipolar modes [30–32]. Higher-order multipolar plasmon resonances have never been systematically investigated, to the best of our knowledge. On the other hand, our transformation approach relates a spheroidal particle to a spherical shell, enabling us to decompose all the eigenmodes in terms of spherical harmonics. As a result, both dipolar and higher-order resonances can be easily addressed using our approach. Moreover, a thin flat disk (finite rod) can be considered as a special case of oblate (prolate) spheroids in the limit of  $b'/a' \ll 1$ . Therefore, we anticipate that the following discussions will be important, especially when people want to make use of the higher-order plasmon modes of disks/rods for further developments.

Figure 4 shows the shifts of the plasmon resonances for oblate and prolate spheroids, again as a function of the ratio between semiminor and semimajor axis ( $b'/a'$ ). As pointed out before, in the 3D case we need two “quantum” numbers,  $l$  (the total angular momentum) and  $m$  (the azimuthal angular momentum) to classify the modes. In the limit of  $b'/a' = 1$ , the resonance condition for both oblate and prolate spheroids is solely determined by the total angular momentum  $l$ , as is

required for a sphere [14]. In the opposite limit of  $b'/a' \rightarrow 0$ , which corresponds to a flat disk for oblate spheroids and a thin rod for prolate spheroids, the behavior is rather different. The modes for oblate spheroids shift to the bulk plasma frequency (corresponds to  $\varepsilon = 0$ ) if  $l - m$  is an odd integer and shift to zero frequency ( $\varepsilon \rightarrow -\infty$ ) if  $l - m$  is an even integer. This behavior can be easily understood through the potential distribution (corresponding to the distribution of surface charges) plotted in the insets of Fig. 4(a) (see Appendix C for higher order modes). When  $l - m$  is an odd (even) number, the surface charges on the upper and bottom surfaces of the spheroidal particle have opposite (the same) signs, and hence the energy of the resonance increases (decreases) for elongated geometries. On the contrary, in the prolate case only the modes with zero azimuthal angular momentum  $m = 0$  shift to zero frequency, while all the other modes shift to the surface plasma frequency ( $\varepsilon = -1$ ). This is because for modes with nonzero  $m$ , the prolate spheroid can be considered as a single cylinder, where all the modes are degenerate at the surface plasmon frequency.

The resonance frequencies of a sphere ( $b'/a' = 1$ ) do not depend on  $m$  [14], yet the modes split for spheroids. In this case, the splitting is due to the breaking of spherical symmetry and the modes can be tuned by changing the ratio of semiminor to semimajor axis. This is similar, but not identical, to tuning the modes in a metal nanoshell with uniform permittivity by changing the shell thickness [33,34]. In our case, the splitting of the modes is not only due to the hybridization of plasmons at the outer and inner surface, but also depends on the angle dependence of the permittivity and permeability.

#### IV. ABSORPTION AND SCATTERING: SELECTION RULE

To identify which of the plasmon modes are bright and which are dark under far-field illumination, we will calculate the absorption and scattering cross sections. The polarizability of the ellipse can be obtained from the scattered part of the potential in the far field [14]. For the ellipse this leads to the polarizability in the quasistatic approximation (see Appendix B),

$$\alpha'_{2d} = -\pi \epsilon_0 \begin{bmatrix} \gamma_{2d}^x & 0 \\ 0 & \gamma_{2d}^y \end{bmatrix} = \begin{bmatrix} \alpha_{2d}^{x'} & 0 \\ 0 & \alpha_{2d}^{y'} \end{bmatrix}, \quad (22)$$

with

$$\gamma_{2d}^x = \frac{(\epsilon'_d - \epsilon'_m) e^{u_0} \cosh(u_0) \sinh(u_0)}{\epsilon'_m \sinh(u_0) + \epsilon'_d \cosh(u_0)}, \quad (23)$$

$$\gamma_{2d}^y = \frac{(\epsilon'_d - \epsilon'_m) e^{u_0} \cosh(u_0) \sinh(u_0)}{\epsilon'_m \cosh(u_0) + \epsilon'_d \sinh(u_0)}. \quad (24)$$

As a result the only bright modes for the ellipse under far-field illumination are the two dipole modes. Higher-order modes would require the presence of terms such as  $\cosh(mu_0)$ ,  $\sinh(mu_0)$ , and  $e^{mu_0}$  in the polarizability. This is a surprising result as at first sight the ellipse does not have enough symmetry to select only these two modes for excitation. The hidden symmetry of the system reveals its hand at this point. Externally incident radiation can couple to the higher order modes but only if the ellipse is large enough to invalidate the quasistatic approximation and so to see the higher multipole terms in the field.

Thus far we have been working in the quasistatic approximation, which limits our treatment to particle sizes of only a few nanometers. However, we can go beyond the quasistatic approximation and account for radiation losses, which greatly increases the maximum size of particles for which this approach is valid [35]. This is done by defining an effective polarizability as [22,35]

$$\alpha_{2d}^{\text{eff},x'/y'} = \frac{\alpha_{2d}^{x'/y'}}{1 - i \frac{k^2}{8} \alpha_{2d}^{x'/y'}}, \quad (25)$$

where  $k$  is the free space wave number of the incident electromagnetic wave. Having obtained the effective polarizability of the ellipse, the extinction  $\sigma_{\text{ext}}$  and scattering  $\sigma_{\text{sca}}$  cross section can be obtained from  $\sigma_{\text{ext}}^{x'/y'} = k \text{Im}(\alpha_{2d}^{\text{eff},x'/y'})$  and  $\sigma_{\text{sca}}^{x'/y'} = \frac{k^3}{8} |\alpha_{2d}^{\text{eff},x'/y'}|^2$  [35,36]. The absorption cross section is then obtained via  $\sigma_{\text{abs}} = \sigma_{\text{ext}} - \sigma_{\text{sca}}$  [36]. Assuming the  $x$  and  $y$  component of the incident electrical field have equal strength, i.e.,  $E'_x = E'_y$ , the total cross sections are simply  $\sigma = \sigma^x + \sigma^y$ .

Figure 5 shows the absorption and scattering cross section for the ellipse illuminated by a plane wave, normalized by the semimajor axis  $a'$  of the ellipse. We assume a silver ellipse in vacuum with permittivity data from Johnson and Christy [18]. Our analytical calculations are compared to simulations obtained with COMSOL MULTIPHYSICS. For particles of semimajor axis  $a' = 5$  nm and  $a' = 10$  nm, theory and simulation are in excellent agreement for both the absorption and scattering cross section. The peaks at  $\approx 2.9$  eV and  $\approx 3.7$  eV correspond to the even and odd dipole resonance of the ellipse. Since there are no other peaks present (for  $a' = 5$  nm and  $a' = 10$  nm),

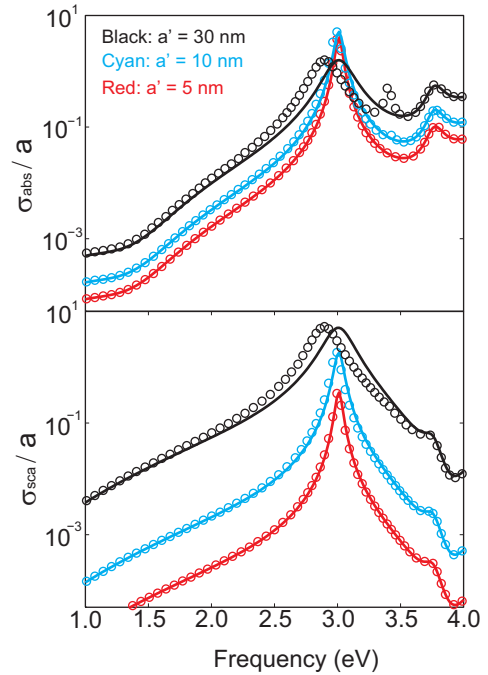


FIG. 5. (Color online) Absorption (top) and scattering (bottom) cross section for the ellipse normalized by its semimajor axis  $a'$ . Shown are the quasistatic results including radiation loss, for our analytic theory (solid lines) and numerical simulations (open circles).

this confirms our selection rule that only the dipole modes can be excited by a plane wave. The origin of this selection rule lies in the rotational symmetry of the annulus and will be exact as long as the quasistatic approximation holds.

As we can see, for particles of semimajor axis  $a' = 30$  nm, the quasistatic approximation starts to break down and the COMSOL simulation shows a peak in the absorption spectrum at the even quadrupole resonance, which the quasistatic approximation cannot predict. Along with the emergence of the quadrupole peak, the dipole peaks in the simulation also redshift compared to our prediction.

Similarly to the 2D case, we can calculate the absorption and scattering cross sections in the 3D case from the polarizability. Assuming an incident potential of the form  $\phi'_{s,3d} = -E_{x'}x' - E_{z'}z'$ , the polarizability is

$$\alpha'_{3d,o/p} = -i \frac{8\pi \epsilon_0}{3E_x} a'_{l=1,m=1}^{\text{sca},o/p}, \quad (26)$$

$$\alpha'_{3d,o/p} = -\frac{4\pi \epsilon_0}{3E_z} a'_{l=1,m=0}^{\text{sca},o/p}, \quad (27)$$

where  $a'_{l,m}^{\text{sca},o/p}$  are the scattering coefficients for oblate and prolate spheroids, respectively [see Eq. (C10) and Eq. (C15)]. The polarizability only has a dipole,  $l = 1$ , response which leads to the same dipole selection rule as in the two-dimensional case.

Incorporating radiation losses as in [22,37] we obtain for the extinction and scattering cross section of the prolate and

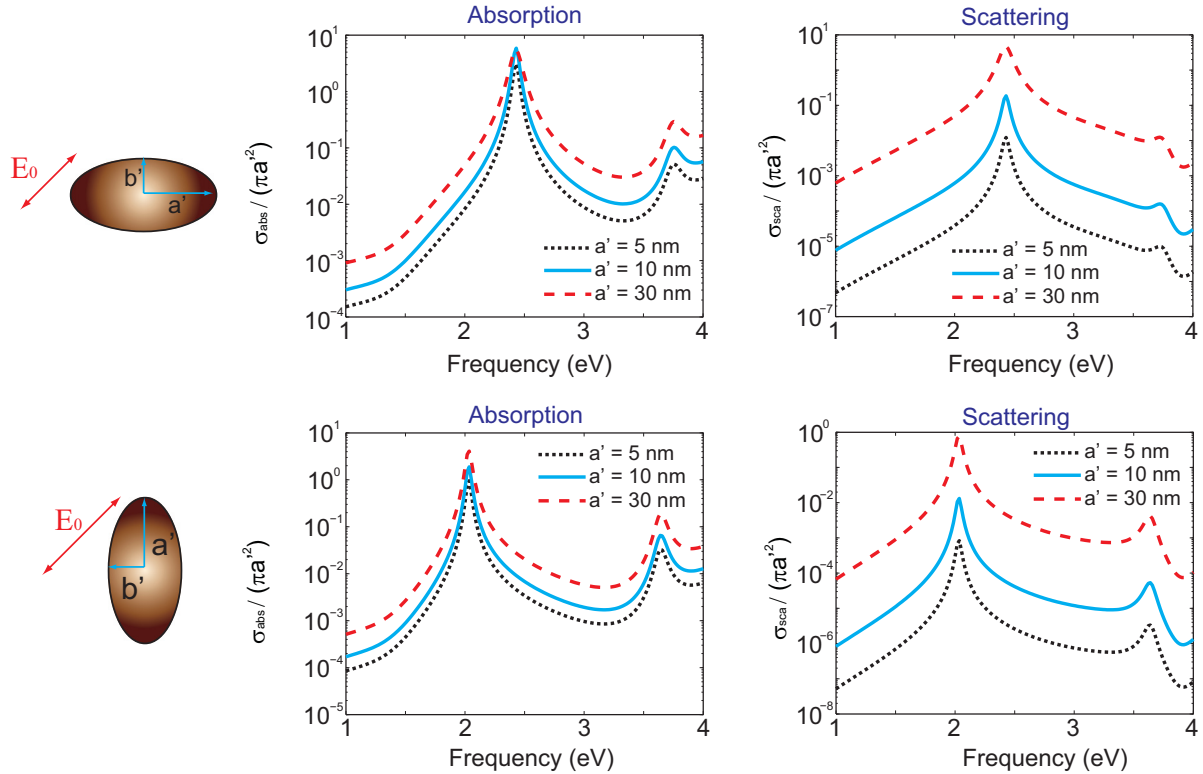


FIG. 6. (Color online) Absorption (left) and scattering (right) cross section for oblate (top) and prolate (bottom) spheroids. The cross sections are normalized by the effective area ( $\pi a^2$ ) of the spheroids. Shown are quasistatic calculations incorporating radiative losses.

oblate spheroid

$$\sigma_{\text{ext}}^{x'/z'} = k \operatorname{Im} \left( \frac{1}{\epsilon_0 / \alpha_{3d,p/o}^{x'/z'} - ik^3 / (6\pi)} \right), \quad (28)$$

$$\sigma_{\text{sca}}^{x'/z'} = \frac{k^4}{6\pi} \left| \frac{1}{\epsilon_0 / \alpha_{3d,p/o}^{x'/z'} - ik^3 / (6\pi)} \right|^2. \quad (29)$$

In the above equations, the imaginary parts of the denominators account for the radiative losses.

The analytical results are shown in Fig. 6, which are normalized by the physical cross section  $\pi a^2$  (detailed comparison with COMSOL simulations are provided in the Appendix C). The dipole modes with  $l = 1$  are again predominant in the absorption/scattering spectrum, providing evidence that our selection rule also holds in the 3D case. Comparing the results shown in Fig. 6, we find that the prolate spheroid is a better candidate for suppressing radiative losses, since the absorption cross section remains one order of magnitude larger than the scattering one even when the semimajor axis  $a'$  increases to 30 nm.

## V. CONCLUSIONS

In this paper, transformation optics has been applied to elliptical nanostructures to study their plasmonic properties in the quasistatic limit and beyond. We have revealed a hidden symmetry in the elliptical structures by transforming them to rotationally (2D) and spherically (3D) symmetric structures, which could be simultaneously diagonalized. This allowed us to classify the original system in terms of the eigenmodes and good “quantum” numbers of the rotationally and spherically symmetric systems. It also explained the

emergence of selection rules in the elliptical geometries based on symmetry arguments in the transformed frame. From a numerical point of view, the symmetries in the transformed frame may allow one to perform quasi-2D or at least quasi-2.5D [38] simulations, instead of more time-consuming 3D simulations. Analytical formulas for the plasmonic resonance conditions in the quasistatic limit of a 2D ellipse and 3D spheroids have been derived, including the ones for a thin strip (2D), a flat disk (3D), and a thin nanorod (3D) as limiting cases. We also calculated the absorption and scattering spectra and have checked our analytical calculations against COMSOL simulations; we found an excellent agreement for particles of diameter  $< 20$  nm. For larger particles the quasistatic approximation and with it the selection rules break down, leading to quadrupole resonances, which provide the starting point of further study.

## ACKNOWLEDGMENTS

The authors wish to thank Dr. Antonio I. Fernandez-Dominguez for fruitful discussions and advice on numerical simulations. This work was supported by the Leverhulme Trust, the Gordon and Betty Moore Foundation, the AFOSR, the EPSRC Active Plasmonics Programme, and the Imperial College Ph.D. scholarship.

## APPENDIX A: TRANSFORMATION OF A DIPOLE SOURCE

In the main text we showed how a constant electric field transforms from the elliptic to the annulus geometry. Here,

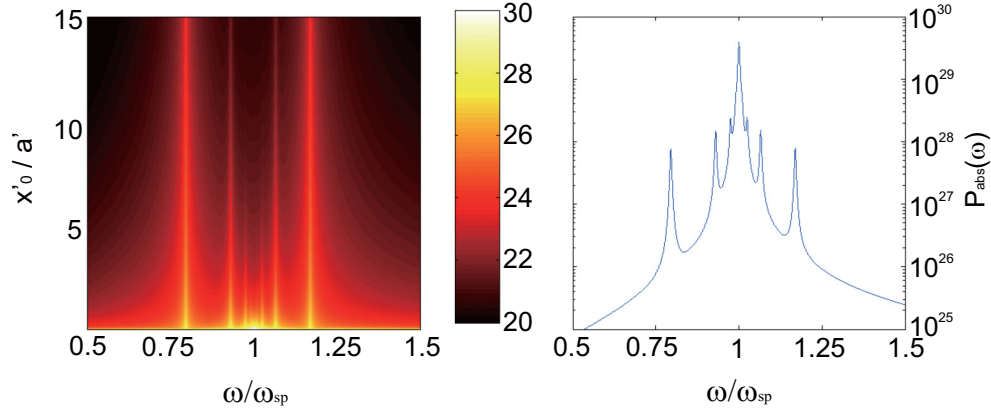


FIG. 7. (Color online) Power absorbed by the annulus in the source field originating from Eq. (A6). This is equivalent to the power absorbed by the ellipse in the corresponding dipole field. The figure on the left shows the  $\log_{10}$ (power absorbed) as a function of frequency and the dipole distance to the ellipse (along  $y$  axis). The figure on the right shows a cut through the left figure along  $x'_0/a' \approx 1.05$ . Note that on the right we show the power absorbed, not  $\log_{10}$ (power absorbed). In both cases the odd/even dipole mode corresponds to the outermost lines/peaks. The power absorbed can be calculated from  $P_{\text{abs}} = -\frac{\omega}{2} \text{Im}(\Delta_- \cdot \mathbf{E}_{\zeta=\zeta_-}^{\text{sca}})$  [22], where  $\mathbf{E}_{\zeta=\zeta_-}^{\text{sca}}$  is the scattered part of the electric field at the position of the dipole at  $\zeta_-$ .

we consider the transformation of a line dipole from elliptic to annulus geometry. The line dipole in the elliptic space is placed along the  $x'$  axis at  $x'_0$ , which results in the source potential

$$\phi'_s = \frac{1}{2\pi\epsilon_0} \frac{\Delta_{x'}(x' - x'_0) + \Delta_{y'}y'}{(x' - x'_0)^2 + (y')^2} \quad (\text{A1})$$

with  $\Delta_{x'} = 2\lambda\delta_{x'}$  and  $\Delta_{y'} = 2\lambda\delta_{y'}$ . To find the source potential in the annulus geometry we first note that the point  $x'_0$  is transformed to two points in the annulus geometry, namely  $x_{\pm} = x'_0/c' \pm \sqrt{(x'_0/c')^2 - 1}$  [inverse of Eq. (2); note that  $x'_0/c' \geq 1$ ]. Further consider how the complex dipole moment

$$\Delta' = \lambda(\zeta'_+ - \zeta'_-) \quad (\text{A2})$$

transforms. Here  $\zeta'_{\pm} = x'_0 \pm (\delta_{x'} + i\delta_{y'})$  gives the position of the positive and negative line charge, respectively. The dipole moment in the annulus geometry is defined in an analogous manner as

$$\Delta = \lambda(\zeta_+ - \zeta_-). \quad (\text{A3})$$

Using the transformation in Eq. (2) of the main text, this can be written to first order in  $(\delta_{x'}, \delta_{y'})$  as

$$\Delta_{\pm} = 2\lambda(\delta_{x'} + i\delta_{y'}) \left( 1 \pm \frac{x'_0/c'}{\sqrt{(x'_0/c')^2 - 1}} \right) \quad (\text{A4})$$

$$= \pm \Delta' \left( \frac{x_{\pm}}{\sqrt{(x'_0/c')^2 - 1}} \right), \quad (\text{A5})$$

which means that a single-line dipole in the elliptic geometry transforms to two-line dipoles in the annulus geometry, one aligned and one antialigned with the original one. Finally the source potential in the annulus geometry can be written as

$$\phi_s = -\frac{1}{2\pi\epsilon_0} \left[ \left( \frac{\Delta_x(x - x_+) + \Delta_y y}{(x - x_+)^2 + y^2} \right) - \left( \frac{\Delta_x(x - x_-) + \Delta_y y}{(x - x_-)^2 + y^2} \right) \right], \quad (\text{A6})$$

with

$$\Delta_{x/y} = \Delta_{x'/y'} \left( \frac{x_{\pm}}{\sqrt{(x'_0/c')^2 - 1}} \right). \quad (\text{A7})$$

The potential problem is then reduced to solving the Laplace equation in polar coordinates with the source potential of (A6). In contrast to the source potential in the main text, the two-line dipoles in the annulus geometry can excite higher-order plasmon modes, as can be seen in Fig. 7. These will then also be present in the elliptic geometry.

## APPENDIX B: CALCULATION OF THE POLARIZABILITY OF THE ELLIPSE

As pointed out in the main text, the polarizability of the ellipse can be calculated from the scattered part of the potential in the far field. The potential outside the ellipse can be obtained in elliptic coordinates  $x' = c' \cosh(u') \cos(v')$ ,  $y' = c' \sinh(u') \sin(v')$  as

$$\begin{aligned} \phi'_{2d} &= \phi'_{s,2d} - \frac{c'}{2} E_{x'} \gamma'_{2d} e^{-u'} \cos(v') - \frac{c'}{2} E_{y'} \gamma'_{2d} e^{-u'} \sin(v') \\ &= \phi'_{s,2d} + \phi'_{\text{sca},2d}, \end{aligned} \quad (\text{B1})$$

where  $\gamma'_{2d}$  and  $\gamma'_{2d}$  are given in the main text. In the far field, the scattered part of the potential above can be rewritten as

$$\begin{aligned} \phi'_{\text{sca},2d} &= -\frac{1}{2} \left( E_{x'} \frac{x'}{x'^2 + y'^2} \gamma'_{2d} + E_{y'} \frac{y'}{x'^2 + y'^2} \gamma'_{2d} \right) \\ &= \frac{1}{2\pi\epsilon_0} \frac{\mathbf{p}'_{2d} \cdot \mathbf{r}'}{r'^2}, \end{aligned} \quad (\text{B2})$$

with the dipole moment of the ellipse

$$\mathbf{p}'_{2d} = -\pi\epsilon_0 \begin{pmatrix} \gamma'_{2d} & 0 \\ 0 & \gamma'_{2d} \end{pmatrix} \begin{pmatrix} E_{x'} \\ E_{y'} \end{pmatrix}. \quad (\text{B3})$$

From the dipole moment in Eq. (B3), we infer the polarizability of the ellipse in the quasistatic approximation as [14]

$$\alpha'_{2d} = -\pi \varepsilon_0 \begin{pmatrix} \gamma'_{2d} & 0 \\ 0 & \gamma'_{2d} \end{pmatrix} = \begin{pmatrix} \alpha'_{2d} & 0 \\ 0 & \alpha'_{2d} \end{pmatrix}. \quad (\text{B4})$$

### APPENDIX C: ANALYTIC SOLUTION TO THE THREE-DIMENSIONAL PROBLEM

*Prolate spheroid.* As shown in the main text, a prolate spheroid can be related to a concentric spherical shell with space-dependent permittivities given by Eqs. (9)–(12) in the main text. Substituting these space-dependent permittivities into  $\nabla \cdot (\bar{\varepsilon} \cdot \nabla \phi) = 0$  and rearranging the equation yields

$$\frac{1}{r^2} \frac{\partial}{\partial r} (1-r^2) \frac{\partial}{\partial r} \phi + \frac{1-r^2}{r^4 \sin \theta} \frac{\partial}{\partial \theta} (\sin \theta) \frac{\partial}{\partial \theta} \phi + \left[ \frac{1-r^2}{r^4 \sin^2 \theta} + \frac{4}{r^2(1-r^2)} \right] \frac{\partial^2}{\partial \varphi^2} \phi = 0. \quad (\text{C1})$$

By letting  $\phi = Z(r)\Xi(\theta)\Phi(\varphi)$ , detailed mathematical manipulations show that Eq. (C1) is separable:

$$\frac{r^2}{1-r^2} \frac{d}{dr} (1-r^2) \frac{dZ}{dr} - \left[ l(l+1) + \frac{4m^2 r^2}{(1-r^2)^2} \right] Z = 0, \quad (\text{C2})$$

$$\frac{1}{\sin \theta} \frac{d}{d\theta} \sin \theta \frac{d\Xi}{d\theta} + \left[ l(l+1) - \frac{m^2}{\sin^2 \theta} \right] \Xi = 0, \quad (\text{C3})$$

$$\frac{d^2 \Phi}{d\varphi^2} = -m^2 \Phi. \quad (\text{C4})$$

The general solution to the above equations can be found as

$$Z(r) = A_1 P_l^m \left[ \frac{1}{2} \left( r + \frac{1}{r} \right) \right] + A_2 Q_l^m \left[ \frac{1}{2} \left( r + \frac{1}{r} \right) \right], \quad (\text{C5})$$

$$\Xi(\theta) = A_3 P_l^m(\cos \theta) + A_4 Q_l^m(\cos \theta), \quad (\text{C6})$$

$$\Phi(\varphi) = A_5 e^{im\varphi} + A_6 e^{-im\varphi}. \quad (\text{C7})$$

It is interesting to see from Eqs. (C6) and (C7) that the solutions for the angular part are still spherical harmonics. On the other hand, Eq. (C5) indicates that the solution for the radial part depends on both total angular momentum  $l$  and azimuthal angular momentum  $m$  (as compared to the case of homogeneous spheres or spherical shells, where only  $l$  appears in the radial solution).

Now, we can write the electrostatic potential in each region. Since the electric field must vanish at the cut  $r = 1$ , this ensures the potential inside the annulus takes the form

$$\phi^{\text{in}} = \sum_{l=1}^{\infty} \sum_{m=-l}^l a_{l,m}^{\text{in}} P_l^m \left[ \frac{1}{2} \left( r + \frac{1}{r} \right) \right] Y_l^m(\theta, \varphi). \quad (\text{C8})$$

Meanwhile, the field must vanish at infinity  $r \rightarrow \infty$ ; this indicates the scattered potential outside the annulus takes the

form

$$\phi^{\text{sca}} = \sum_{l=1}^{\infty} \sum_{m=-l}^l a_{l,m}^{\text{sca}} \left\{ i \frac{\pi}{2} P_l^m \left[ \frac{1}{2} \left( r + \frac{1}{r} \right) \right] + Q_l^m \left[ \frac{1}{2} \left( r + \frac{1}{r} \right) \right] \right\} Y_l^m(\theta, \varphi). \quad (\text{C9})$$

By solving the boundary equations, the unknown expansion coefficients  $a_{l,m}^{\text{sca}}$  and  $a_{l,m}^{\text{in}}$  can be calculated:

$$a_{l,m}^{\text{sca}} = \frac{(\varepsilon - 1) P_l^m(\tau) P_l^{m'}(\tau)}{P_l^m(\tau) G_l^{m'}(\tau) - \varepsilon G_l^m(\tau) P_l^{m'}(\tau)} a_{l,m}^{\text{S}}, \quad (\text{C10})$$

$$a_{l,m}^{\text{in}} = \frac{P_l^m(\tau) G_l^{m'}(\tau) - G_l^m(\tau) P_l^{m'}(\tau)}{P_l^m(\tau) G_l^{m'}(\tau) - \varepsilon G_l^m(\tau) P_l^{m'}(\tau)} a_{l,m}^{\text{S}}, \quad (\text{C11})$$

where we have defined  $\tau = (R^{\text{out}} + 1/R^{\text{out}})/2$  and  $G_l^m(\cdot) = i\pi P_l^m(\cdot)/2 + Q_l^m(\cdot)$ .

*Oblate spheroid.* The solution to the oblate spheroid can be derived in a similar manner. We first submit Eqs. (13)–(16) in the main text into  $\nabla \cdot (\bar{\varepsilon} \cdot \nabla \phi) = 0$ , yielding

$$\frac{1}{r^2} \frac{\partial}{\partial r} (1+r^2) \frac{\partial}{\partial r} \phi + \frac{1+r^2}{r^4 \sin \theta} \frac{\partial}{\partial \theta} \sin \theta \frac{\partial}{\partial \theta} \phi + \left[ \frac{1+r^2}{r^4 \sin^2 \theta} - \frac{4}{r^2(1+r^2)} \right] \frac{\partial^2}{\partial \varphi^2} \phi = 0. \quad (\text{C12})$$

By solving Eq. (C12), we can list the scattered potential and the potential inside the annulus region as

$$\phi^{\text{sca}} = \sum_{l=1}^{\infty} \sum_{m=-l}^l a_{l,m}^{\text{sca}} F_l^m \left[ i \left( r - \frac{1}{r} \right) \right] P_l^m(\cos \theta) e^{im\varphi}, \quad (\text{C13})$$

$$\phi^{\text{in}} = \sum_{l=1}^{\infty} \sum_{m=-l}^l a_{l,m}^{\text{in}} P_l^m \left[ i \left( r - \frac{1}{r} \right) \right] P_l^m(\cos \theta) e^{im\varphi}, \quad (\text{C14})$$

where we have defined a function  $F_l^m(\cdot) = -i\pi P_l^m(\cdot)/2 + Q_l^m(\cdot)$ . Solving the boundary conditions,  $a_{l,m}^{\text{sca}}$  and  $a_{l,m}^{\text{in}}$  can be obtained:

$$a_{l,m}^{\text{sca}} = \frac{(\varepsilon - 1) P_l^m(i\xi) P_l^{m'}(i\xi)}{P_l^m(i\xi) F_l^{m'}(i\xi) - \varepsilon F_l^m(i\xi) P_l^{m'}(i\xi)} a_{l,m}^{\text{S}}, \quad (\text{C15})$$

$$a_{l,m}^{\text{in}} = \frac{P_l^m(i\xi) F_l^{m'}(i\xi) - F_l^m(i\xi) P_l^{m'}(i\xi)}{P_l^m(i\xi) F_l^{m'}(i\xi) - \varepsilon F_l^m(i\xi) P_l^{m'}(i\xi)} a_{l,m}^{\text{S}}, \quad (\text{C16})$$

where we have defined a constant  $\xi = (R^{\text{out}} - 1/R^{\text{out}})/2$ .

*Absorption and scattering cross sections for spheroidal particles.* Taking the oblate spheroid as the example, for plane wave illuminations, we have the following relation:

$$\phi^{\text{S}} = E_x x + E_z z = a_{1,1}^{\text{S}} x + i a_{1,0}^{\text{S}} z. \quad (\text{C17})$$

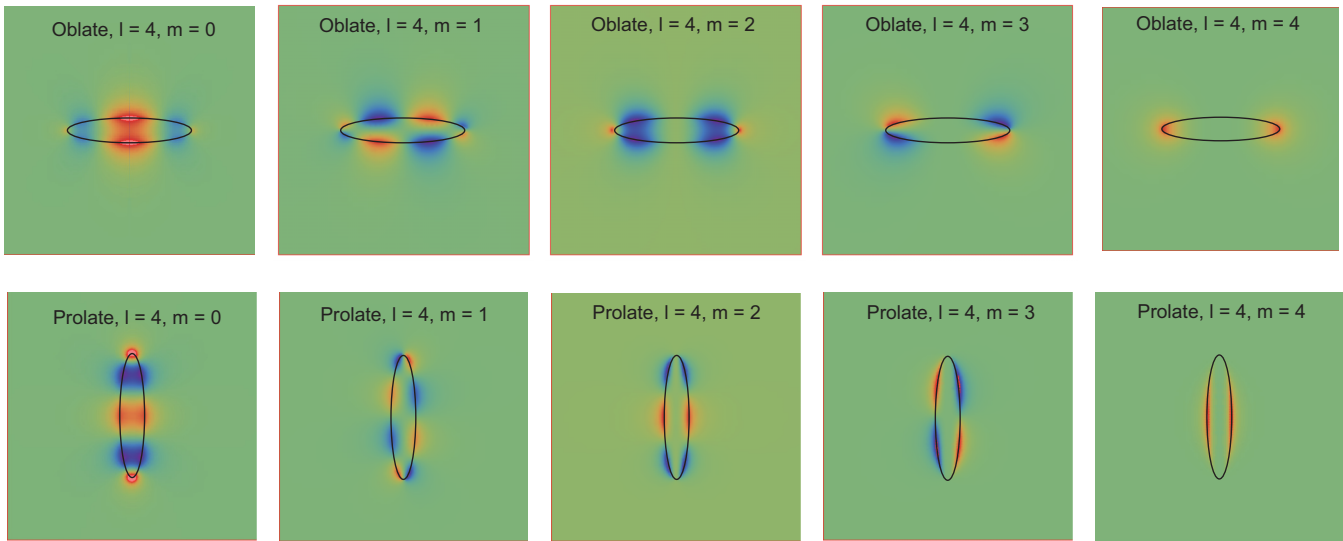


FIG. 8. (Color online) Imaginary part of the electrostatic potential for oblate (upper) and prolate (bottom) spheroids at different resonant frequencies. Here the total angular momentum is fixed as  $l = 4$ . Different columns correspond to different angular momenta  $m$  (from 0 to 4).

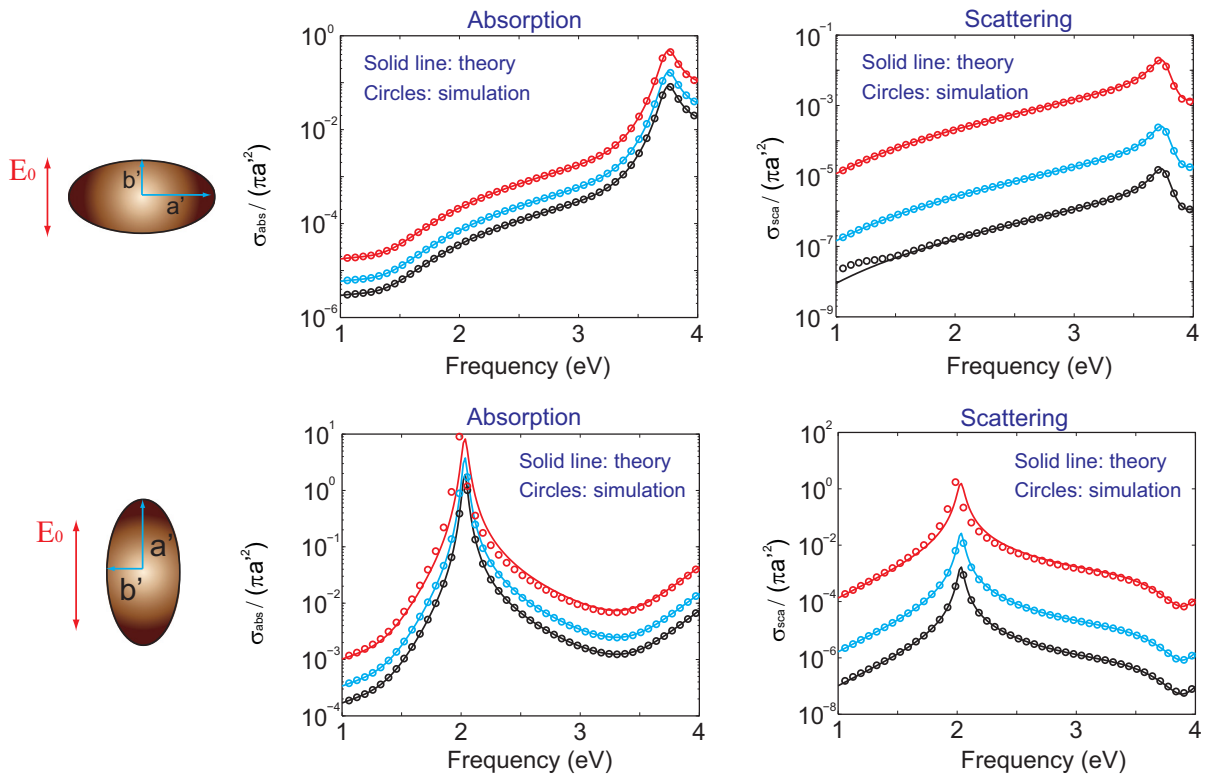


FIG. 9. (Color online) Absorption (left) and scattering (right) cross section for oblate (top) and prolate (bottom) spheroids. The cross sections are normalized by the effective area ( $\pi a'^2$ ) of the spheroids. The incident electric field is aligned along the vertical direction. Solid lines show our theoretical calculation, while circles correspond to COMSOL simulations. Different colors correspond to structures with different dimensions: black ( $a' = 5$  nm), cyan ( $a' = 10$  nm), red ( $a' = 30$  nm).

The expansion coefficients associated with the source potential can then be obtained:

$$a_{1,1}^S = E_x, a_{1,0}^S = -iE_z. \quad (\text{C18})$$

The polarizability is related to the scattered potential at infinity:

$$\begin{aligned} \phi^{\text{sca}}(r' \rightarrow \infty) &= a_{1,0}^{\text{sca}} F_1^0 \left[ i \left( r - \frac{1}{r} \right) \right] \cos \theta \\ &\quad - a_{1,1}^{\text{sca}} F_1^1 \left[ i \left( r - \frac{1}{r} \right) \right] \sin \theta \cos \varphi \\ &= -\frac{2i a_{1,1}^{\text{sca}}}{3r'^3} x - \frac{a_{1,0}^{\text{sca}}}{3r'^3} z = \frac{1}{4\pi\epsilon_0} \frac{\gamma_x E_x x + \gamma_z E_z z}{r'^3}. \end{aligned} \quad (\text{C19})$$

From the above equation, we can calculate the polarizability:

$$\gamma_x = -i \frac{8\pi\epsilon_0}{3E_x} a_{1,1}^{\text{sca}}, \quad \gamma_z = -\frac{4\pi\epsilon_0}{3E_z} a_{1,0}^{\text{sca}}. \quad (\text{C20})$$

Equation (C20) in turn gives the absorption and scattering cross sections [37]:

$$\sigma_{\text{abs}}^c = k_0 \text{Im} \left\{ \frac{1}{\epsilon_0/\gamma - ik_0^3/(6\pi)} \right\}, \quad (\text{C21})$$

$$\sigma_{\text{sca}}^c = \frac{k_0^4}{6\pi} \left| \frac{1}{\epsilon_0/\gamma - ik_0^3/(6\pi)} \right|^2. \quad (\text{C22})$$

*Results.* Figure 8 shows the electrostatic potential as calculated above. Shown are the distributions for oblate and prolate spheroids with total angular momentum  $l = 4$  and azimuthal angular momentum  $m$  ranging from 0 to 1. As discussed in the main text, this explains the shifting of the plasmon resonance frequencies of Fig. 4. Figure 9 compares the analytical calculation of the absorption and scattering spectra with numerical simulations obtained from COMSOL MULTIPHYSICS. For both prolate and oblate spheroids excellent agreement is found for particles with semimajor  $a' = 5, 10$ , and 30 nm.

- 
- [1] A. J. Ward and J. B. Pendry, *J. Mod. Opt.* **43**, 773 (1996).  
[2] J. B. Pendry, D. Schurig, and D. R. Smith, *Science* **312**, 1780 (2006).  
[3] Ulf Leonhardt, *Science* **312**, 1777 (2006).  
[4] U. Leonhardt and T. G. Philbin, *Prog. Opt.* **53**, 69 (2009).  
[5] H. Y. Chen, C. T. Chan, and P. Sheng, *Nat. Mater.* **9**, 387 (2010).  
[6] J. B. Pendry, A. Aubry, D. R. Smith, and S. A. Maier, *Science* **337**, 549 (2012).  
[7] Y. Luo, R. Zhao, A. I. Fernandez-Dominguez, S. A. Maier, and J. B. Pendry, *Sci. China Inf. Sci.* **56**, 120401 (2013).  
[8] Charles Kittel, *Introduction to Solid State Physics*, 6th ed. (John Wiley & Sons, Inc., New York, 1986).  
[9] Y. Luo, D. Y. Lei, S. A. Maier, and J. B. Pendry, *Phys. Rev. Lett.* **108**, 023901 (2012).  
[10] J. Zhang and A. V. Zayats, *Opt. Express* **21**, 8426 (2013).  
[11] Roland Schinzinger and Patricio A. A. Laura, *Conformal Mapping—Methods and Applications* (Dover Publications, Inc., Minealo, NY, 2003).  
[12] A. Aubry and J. B. Pendry, *Active Plasmonics and Tuneable Plasmonic Metamaterials*, 1st ed., edited by A. V. Zayats and S. A. Maier (John Wiley & Sons, Inc., Hoboken, NJ, 2013), Chap. 4, pp. 105–152.  
[13] E. N. Economou, *Phys. Rev.* **182**, 539 (1969).  
[14] S. A. Maier, *Plasmonics: Fundamentals and Applications* (Springer, New York, 2007).  
[15] Richard Feynman, Robert Leighton, and Matthew Sands, *The Feynman Lectures on Physics*, 2nd ed., Vol. 2 (Addison-Wesley, Boston, 1963).  
[16] J. B. Pendry, A. I. Fernandez-Dominguez, Y. Luo, and R. Zhao, *Nat. Phys.* **9**, 518 (2013).  
[17] John D. Jackson, *Classical Electrodynamics*, 3rd. ed. (Wiley, New York, 1998).  
[18] P. B. Johnson and R. W. Christy, *Phys. Rev. B* **6**, 4370 (1972).  
[19] Philip M. Mores and Hermann Feshbach, *Methods of Theoretical Physics, Part II* (McGraw-Hill Book Company, Inc., New York, 1953).  
[20] Joerg Kottmann, Olivier Martin, David Smith, and Sheldon Schultz, *Opt. Express* **6**, 213 (2000).  
[21] Eloneid F. Vasconcelos, Newton T. de Oliveira, and Gil A. Farias, *Phys. Rev. B* **44**, 13740 (1991).  
[22] L. Novotny and B. Hecht, *Principles of Nano-Optics* (Cambridge University Press, Cambridge, UK, 2006).  
[23] P. Nordlander and E. Prodan, *Nano Lett.* **4**, 2209 (2004).  
[24] E. Prodan, C. Radloff, N. J. Halas, and P. Nordlander, *Science* **302**, 419 (2003).  
[25] K. M. Siegel, F. V. Schultz, B. H. Gere, and F. B. Sleanor, *IRE Trans. Antennas Propag.* **4**, 266 (1956).  
[26] B. P. Sinha and R. H. MacPhie, *IEEE Trans. Antennas Propag.* **23**, 676 (1975).  
[27] N. V. Voshchinnikov and V. G. Farafonov, *Meas. Sci. Technol.* **13**, 249 (2002).  
[28] B. P. Sinha and R. H. MacPhie, *Radio Sci.* **12**, 171 (2012).  
[29] A. D. Kotsis and J. A. Roumeliotis, *Prog. Electromagn. Res.* **67**, 113 (2007).  
[30] S. J. Norton and T. Vo-Dinh, *IEEE Trans. Nanotechnol.* **6**, 627 (2007).  
[31] N. I. Grigorchuk, *Europhys. Lett.* **97**, 45001 (2012).  
[32] J. J. Penninkhof, A. Moroz, A. van Blaaderen, and A. Polman, *J. Phys. Chem. C* **112**, 4146 (2008).  
[33] S. J. Oldenburg, R. D. Averitt, S. L. Westcott, and N. J. Halas, *Chem. Phys. Lett.* **288**, 243 (1998).  
[34] E. Prodan and P. Nordlander, *Nano Lett.* **3**, 543 (2003).  
[35] A. Aubry, D. Y. Lei, S. A. Maier, and J. B. Pendry, *Phys. Rev. B* **82**, 205109 (2010).  
[36] Craig F. Bohren and Donald R. Huffman, *Absorption and Scattering of Light by Small Particles* (Wiley-VCH, Weinheim, Germany, 2004).  
[37] Y. Luo, Ph.D. thesis, Imperial College London, 2012.  
[38] C. Ciraci, R. T. Hill, J. J. Mock, Y. Urzhumov, A. I. Fernandez-Dominguez, S. A. Maier, J. B. Pendry, A. Chilkoti, and D. R. Smith, *Science* **337**, 1072 (2012).